OPEN ACCESS

University of BRISTOL

Peer reviewed version

Link to published version (if available):
10.1016/j.ndteint.2015.12.009

Link to publication record in Explore Bristol Research
PDF-document

University of Bristol - Explore Bristol Research
General rights

Ultrasonic Array Imaging Through an Anisotropic Austenitic Steel Weld Using an Efficient Ray-tracing Algorithm

Oliver Nowers[a,b], David Duxbury[a], B. W. Drinkwater[b]

[a]*NDE Research, Rolls-Royce, Derby, PO BOX 2000*
[b]*Department of Mechanical Engineering, University of Bristol, University Walk, Bristol, BS8 1TR*

Abstract

Ultrasonic inspection of austenitic welds is challenging due to their highly anisotropic and heterogeneous microstructure. The weld anisotropy causes a steering of the ultrasonic beam leading to a number of adverse effects upon ultrasonic array imagery, including defect mislocation and aberration of the defect response. A semi-analytical model to simulate degraded ultrasonic images due to propagation through an anisotropic austenitic weld is developed. Ray-tracing is performed using the A* path-finding algorithm and integrated into a semi-analytical beam-simulation and imaging routine to observe the impact of weld anisotropy on ultrasonic imaging. Representative anisotropy weld-maps are supplied by the MINA model of the welding process. A number of parametric studies are considered, including the magnitude and behaviour of defect mislocation and amplitude as the position of a fusion-face defect and the anisotropy distribution of a weld is varied, respectively. Furthermore, the use of the model to efficiently simulate and evaluate ultrasonic image degradation due to anisotropic austenitic welds during an inspection development process is discussed.

Keywords: Ultrasonics, anisotropy, austenitic welds, ray-tracing

1. Introduction

Within the nuclear power generation industry, ultrasonic Non-Destructive Evaluation (NDE) is employed as a means to verify the structural integrity of a given component at a manufacturing stage and at various points throughout its operational life. Due to the safety-critical nature of the industry, the ability to accurately detect, characterize and size defects is of paramount importance. Ultrasonic NDE of austenitic welds is particularly challenging due to their highly anisotropic and heterogeneous microstructures [1]. One of the principal anisotropic effects occurs when ultrasound passing through a weld is 'bent' in a process known as 'beam-steering' [2]. Since it is common practise to assume material isotropy during ultrasonic inspections, this can lead to a variety of problems during ultrasonic array inspection of anisotropic and heterogeneous materials, including the mislocation of defects, and aberration of the defect response. In turn, this can lead to a reduced Probability of Detection and an increased Probability of a False Alarm, influencing both the quality of the inspection and the confidence placed in its results. The degree of defect mislocation and degradation may be a function of inspection parameters such as the probe position, the beam angle, the number and distribution of array elements, the weld anisotropy, the defect location and many more. As such, the ability to model beam-steering and its impact upon ultrasonic imaging allows a qualitative and quantitative assessment of the impact of anisotropy of a particular weld upon a given ultrasonic inspection, and more importantly, the potential to optimise the inspection through parametric analysis or an optimisation framework e.g. simulated annealing or genetic algorithms [3, 4, 5, 6].

A key aspect to the modelling of defect aberration due to wave prop-

agation in an anisotropic weld is the calculation of the ray-path and its deviations as it progresses through the anisotropic weld metal. Two modelling strategies commonly applied to the modelling of anisotropic wave propagation include use of the Finite Element Method (FEM) and also a semi-analytical method that draws upon a ray-tracing tool. The FEM is a robust and well-established tool for the simulation of wave propagation and defect interaction in materials, and has seen widespread use in the modelling of wave propagation in austenitic welds. Fellinger et al. [7] first adapted the Elastodynamic Finite Integration Technique (EFIT) from electromagnetics to ultrasonics for anisotropic heterogeneous media in 3D. The EFIT technique relies upon the discretisation of the underlying elastodynamic equations for ultrasonic propagation and Fellinger et al. considered various two-dimensional NDE problems with snapshots of the wave propagation at various time intervals. Halkjaer et al [8] used the EFIT in tandem with the Ogilvy weld model [9] for an austenitic weld, assuming a transversely isotropic material, demonstrating good agreement between experimental and simulated A-scans, while Hannemann et al. [10] applied the EFIT to the inspection of an idealised V-butt weld with good qualitative agreement between experimental and simulated B-scans. Langenberg et al. [11] also used the EFIT with validation against a weld transmission experiment using a simplified symmetrical weld structure. Chassignole et al. [12] developed the 2D finite element code, ULTSON, to predict ultrasonic wave propagation in anisotropic and heterogeneous media. Chassignole discretised an austenitic weld into twelve homogeneous domains and determined the columnar grain direction from X-ray Diffraction analysis and Electron Back-scattered Diffraction analysis. Apfel et al. [13] developed the 2D finite element propagation code, ATHENA, using a fictitious domain method such

that a regular mesh of the calculation domain could be combined with an irregular mesh of the defect domain, allowing a superior computation speed. This work was further developed to analyse attenuation of the beam [14], comparison to the pulse-echo amplitude of Side-Drilled-Holes in a mock-up weld [15], and structural noise in a multiple-scattering environment [16]. More recently, the ATHENA code has been extended to 3D [17] showing good agreement with the modelling tool CIVA [18] in isotropic and heterogeneous media. However, FEM approaches suffer from extended computation times and physical memory limitations, especially if a large simulation domain is required, for example a large 3-D weld inspection scenario. Furthermore, accurate simulation of various inspection setups is non-trivial, for instance, the modelling of an immersion inspection where accurate simulation of the fluid/solid interface would be required.

Semi-analytical methods require the modelling of each aspect of the ultrasonic test, including transducer simulation, beam propagation and beam-defect interaction. Beam propagation is modelled through use of a ray-tracing algorithm, which, as applied to ultrasonic NDE, is able to predict the path of a wave during propagation through an arbitrary medium. As such, ray-tracing algorithms are particularly useful for the prediction of wave propagation in heterogeneous and anisotropic materials, where the wave path is non-trivial and subject to deviations. Typically, the wave is 'traced' in the direction of maximum group velocity i.e. the energy flow. A number of ray-tracing algorithms exist for a wide variety of applications [9, 19, 20] and principally differ in their treatment of ray properties. In general, ray-tracing algorithms that consider many ray properties during propagation e.g. velocity, amplitude, polarisation etc. may be computationally slower than those that consider only basic ray properties e.g. velocity. For this

4

reason, the choice of ray-tracing algorithm is an important consideration and is dependent upon the exact requirements of the situation in which the ray-tracing algorithm will be used.

Historically, ray-tracing algorithms as applied to austenitic weld inspection have fulfilled a number of applications, including the modelling of wave paths to determine weld coverage [20, 21, 22, 23], analysis of reflection properties of defects within welds [9], and the correction of degraded images due to wave propagation through austenitic welds [20, 5]. This paper, however, concerns the novel use of the A* 'path-finding' ray-tracing algorithm to simulate degraded ultrasonic array images due to propagation through austenitic weld material. The paper also presents analysis of the characteristics of the degradation when key inspection parameters are varied through parametric analysis. Due to its improved computation speed as compared to the FEM, and ability to model a diverse range of inspection requirements (e.g. varying transducer types), a semi-analytical methodology is desirable as it is potentially necessary to conduct many thousands of ray-traces during a parametric study.

2. Ray-tracing Algorithms

There are generally two types of ray-tracing algorithm as applied to ultrasonic NDE: 'marching' methods and 'minimisation' methods. Marching methods rely upon the principle of 'marching' a ray a through a fixed time or distance interval coupled with iterative solution of the wave properties at each increment, while minimisation methods operate through the minimisation of the time-of-flight between two arbitrary points.

One of the first marching methods as applied to the prediction of beam-

5

steering effects in anisotropic and heterogeneous materials was developed by Silk [24]. A source position is chosen and a ray is propagated at a given angle and velocity until a material interface is reached. At each step, the ray properties are then calculated dependent upon the local material properties either side of the boundary, and the procedure repeated until a ray-trace is formed. Ogilvy [21] developed the software RAYTRAIM, where a ray is moved in discrete distance intervals along its trajectory. At each step, an imaginary interface is created and the local material properties analysed to solve for the on-going ray. Both the wave amplitude and direction are predicted, however this can lead to lengthy computation times should a ray be required to propagate a long distance or to a specific termination point. Schmitz et al. [25] adapted Ogilvy's work to step a ray along discrete time intervals and developed a 3D ray-tracing tool for austenitic materials with good agreement between simulation and experiment when considering the modified beam-spread effect through an austenitic electron-beam weld. Connolly et al. addressed the difficulty of tracing to a desired termination point through adaptation of Ogilvy's work and implementation of a procedure to iteratively adjust the 'launch' angle of a ray until the ray terminates at the desired point in a trial-and-error approach [20]. This is particularly useful for array imaging where a specific ray creation and ray termination point are required e.g. transmitting array element to a receiving array element via a defect or back-wall. However, the algorithm can suffer from extended computation times due to the potential need for many trial launch angles before the correct termination point is achieved.

Minimisation methods operate based upon Fermat's principle of minimum time stating that a wave will propagate between two arbitrary points in space such that the time of propagation between the two is a minimum.

A common example is the beam-bending method [19], which relies upon the iterative 'bending' of a spline curve between two points such that the total time-of-flight along the spline is minimised. Since the algorithm does not explicitly involve the calculation of wave properties (e.g. amplitude, polarisation etc.) the algorithm benefits from a dramatically reduced computation time as compared to typical marching methods. Path-finding algorithms are a subset of minimisation methods, predominantly used within computer science applications but which have seen increased uptake into the field of NDE [5, 26]. The A* algorithm is a computationally rapid path-finding algorithm and enables ray-tracing between two specified points through the connection of a number of nodes whose position is defined by the user. Unique to its operation is the use of 'heuristics', whereby knowledge of the termination point is used to inform the progression of the algorithm. This may be exploited to yield a solution for a given ray-trace in a very short amount of time, making the algorithm ideal for the model described in this paper, where many thousands of ray-traces may be required for a parametric study.

The beam-steering model described in this paper consists of four major parts: (1) weld simulation, (2) ray-tracing, (3) defect simulation and (4) beam-simulation and imaging. As detailed in Section 3.1, the weld simulation step concerns the specification of the weld anisotropy, and its material parameters such that the velocity of propagation may be calculated across the weld. Ray-tracing is performed using the A* algorithm [27] as detailed in Section 3.2, to obtain the time-of-flight for each array element combination to and from the defect. As given in Section 3.3, the scattering behaviour of the defect is encapsulated through use of the scattering matrix (or S-matrix) associated with the defect, describing the far-field scattering amplitude as a function of the incident and scattered angles, and the ultrasonic wavelength

7

[28]. Finally, as detailed in Section 3.4, the Full-Matrix-Capture (FMC) of transmit-receive data [29] is created in the beam simulation step, and an imaging algorithm applied to allow analysis of defect mislocation and aberration due to weld anisotropy.

3. Methodology

3.1. Weld simulation

A 'weld-map' is a useful descriptor of material anisotropy, and indicates the local anisotropic orientation as a function of position in the weld. A number of models exist for the description of anisotropy in austenitic welds [9, 24, 25, 30]. Silk [24] divided a 2D section of the weld-region into a number of quadrilateral areas each with its own anisotropic orientation. The anisotropy of each region was then specified according to the user. Ogilvy [9] described the modelling of Manual Metal Arc (MMA) welds, predicting columnar grain growth perpendicular to the isotherms as the weld cools. Schmitz et al. [25] drew upon a simple linear description of grain orientation as a function of the position in the weld. However, both the Ogilvy and Schmitz models rely upon an axis of symmetry along the weld centre-line and are unable to describe asymmetric local variations in anisotropic orientation as a result of the welding sequence. Furthermore, the models are generic and cannot be tailored towards a specific welding scenario. The MINA model (Modelling anIsotropy through the Notebook of Arc-welding) described by Moysan et al. [30] can be tailored towards a specific weld and draws upon measurements made from a macrograph of the weld and knowledge of welding parameters and sequencing to predict the weld anisotropy. As such, the model is able to account for anisotropy

variation on a weld-by-weld basis. There are five key inputs to the MINA model. The re-melting rates govern the extent to which one weld-pass re-melts a previous weld-pass and includes the lateral re-melting rate, R_L, defined as the ratio of the re-melted width of the current weld-pass due to deposition of the next weld-pass and its total width, and the vertical re-melting rate, R_V, defined as the ratio of the re-melted height of the current weld-pass due to deposition of the weld-pass above, and its total height. The inclination angles govern the tilt of each weld-pass, and include the chamfer inclination, θ_B, and the weld-pass inclination, θ_C, defined as the angles of inclination of the symmetry axis of the weld-pass to the vertical when the weld-pass is against the edge of the chamfer, or another weld-pass, respectively. Finally, the sequencing order of weld-passes must be included to account for variation induced by differing welding procedures. In this way, the MINA model can be used to predict the weld anisotropy on a case-by-case basis. The MINA model is used to determine the weld anisotropy for all scenarios considered in this paper.

Since ray-tracing is performed using a time-minimisation approach, knowledge of the associated propagation velocities of each section of the weld is crucial to the accuracy of the final ray-trace. The Christoffel equation governs the relationship between the stiffness matrix of a medium and its principal propagation velocities. For a general anisotropic solid, the triclinic form of the Christoffel equation is given as:

$$k^2 \begin{bmatrix} \alpha & \delta & \epsilon \\ \delta & \beta & \xi \\ \epsilon & \xi & \gamma \end{bmatrix} \begin{bmatrix} u_x \\ u_y \\ u_z \end{bmatrix} = \rho \omega^2 \begin{bmatrix} u_x \\ u_y \\ u_z \end{bmatrix} \tag{1}$$

9
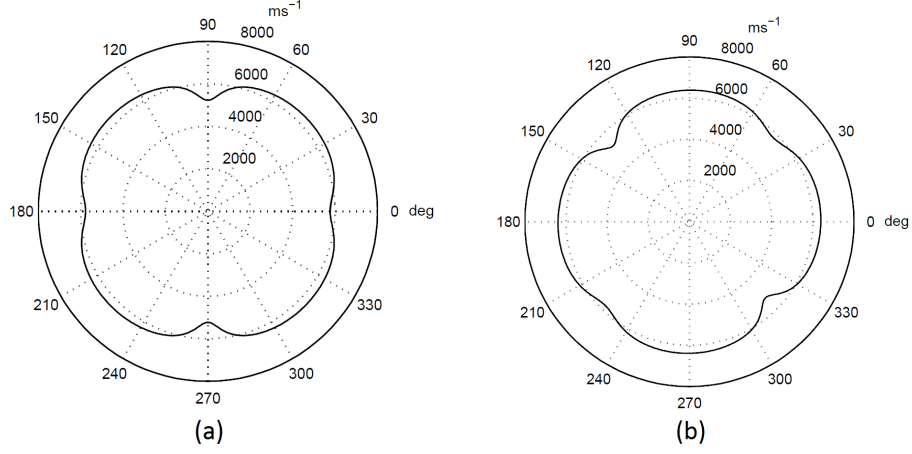
Figure 1: Variation of longitudinal wave velocity as a function of the incident angle for an anisotropic orientation of (a) 0° and (b) 45°.

where ω is the angular frequency, k is the wavenumber, ρ is the density and $\mathbf{u}$ is the particle displacement vector expressed in terms of the three orthogonal Cartesian axes, (x, y, z). The square matrix, or Christoffel matrix, is a construction of elastic stiffness constants [2] given by:

$$\alpha = c_{11}l_x{}^2 + c_{66}l_y{}^2 + c_{55}l_z{}^2 + 2c_{56}l_yl_z \\ + 2c_{15}l_zl_x + 2c_{16}l_xl_y \tag{2}$$

$$\beta = c_{66}l_x{}^2 + c_{22}l_y{}^2 + c_{44}l_z{}^2 + 2c_{24}l_yl_z \\ + 2c_{46}l_zl_x + 2c_{26}l_xl_y \tag{3}$$

10

$$\gamma = c_{55}l_x{}^2 + c_{44}l_y{}^2 + c_{33}l_z{}^2 + 2c_{34}l_yl_z$$
$$+2c_{35}l_zl_x + 2c_{45}l_xl_y \tag{4}$$

$$\delta = c_{16}l_x{}^2 + c_{26}l_y{}^2 + c_{45}l_z{}^2 + (c_{46} + c_{25})l_yl_z$$
$$+(c_{14} + c_{56})l_zl_x + (c_{12} + c_{66})l_xl_y \tag{5}$$

$$\epsilon = c_{15}l_x{}^2 + c_{46}l_y{}^2 + c_{35}l_z{}^2 + (c_{45} + c_{36})l_yl_z$$
$$+(c_{13} + c_{55})l_zl_x + (c_{14} + c_{56})l_xl_y \tag{6}$$

$$\xi = c_{56}l_x{}^2 + c_{24}l_y{}^2 + c_{34}l_z{}^2 + (c_{44} + c_{23})l_yl_z$$
$$+(c_{36} + c_{45})l_zl_x + (c_{25} + c_{46})l_xl_y \tag{7}$$

where c_{mn} is the corresponding elastic constant and direction cosines, $l_{x,y,z}$, are given by:

$$l_{x,y,z} = \frac{k_{x,y,z}}{k} \tag{8}$$

As such, once the material elastic constants and weld anisotropy have been specified, the Christoffel equations may be used to calculate the velocity variation associated with the particular anisotropic orientation and incident angle of the wave [2]. Ray-tracing may then be performed as detailed in Section 3.2. Figure 1 illustrates an example longitudinal velocity variation for austenitic steel as a function of the incident angle for an anisotropic

11

orientation of 0° and 45°.

3.2. Ray-tracing routine

The ray-tracing routine calculates the time-of-flight between the desired creation point e.g. array element and termination point e.g. defect. The model assumes reciprocity, such that the time-of-flight between two given points is identical for a ray propagating in either direction. This is a reasonable assumption due to the 2-fold or higher symmetry exhibited in the velocity curves of stainless steels (SS), as given in Figure 1.

Due to its improved computation speed, the A* algorithm is chosen to perform ray-tracing for the given weld anisotropy input. The A* algorithm [27] is a modified version of Dijkstra's algorithm [31], which was originally conceived as a solution to the 'Travelling Salesman Problem' [32]. As detailed in Figure 2, two adjacent regions, R_1 and R_2, are defined, each with their own anisotropic orientation, ϕ_1 and ϕ_2, respectively. Two nodes, n_1 and n_2, located in R_1 and R_2, respectively, are now defined. The 'nodal cost', $g(n)$, refers to the cost to the algorithm to propagate from n_1 to n_2, and which corresponds to the particular metric to be minimised. For this paper, the cost is taken to be the corresponding time-of-flight. Therefore, the time of propagation between the two nodes, t_{12}, is equivalent to $g(n)$, and is dependent upon the distance between the nodes, d_{12}, and the propagation velocity, c_1, associated with R_1, which is a function of the local anisotropic orientation and the angle between the two nodes, θ, as:

$$t_{12} = \frac{d_{12}}{c_1(\phi_1, \theta)} \tag{9}$$

The velocity in the denominator of Equation (9) may be either that associated with R_1, R_2, or a combination of the two. For all cases discussed
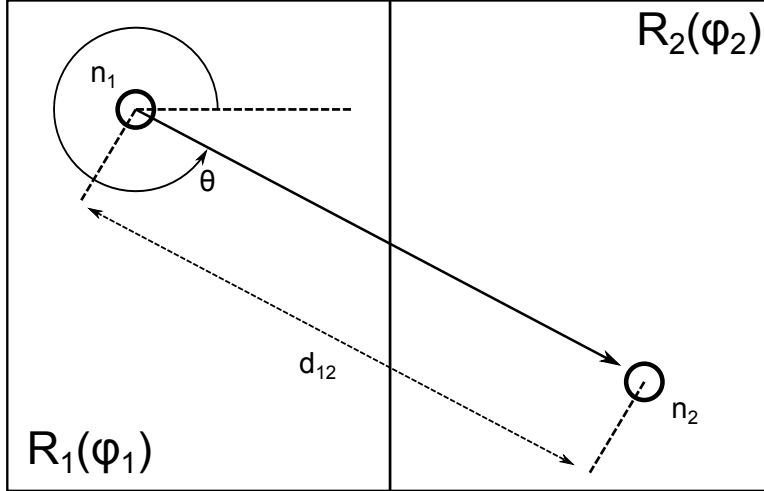
12

Figure 2: Illustration of a ray-trace between two nodes in different anisotropic sub-regions.

in this paper, the velocity used is that associated with the initial sub-region for the given ray-jump. Following this principle, the system may be extended to an arbitrary number of nodes, n_1 to n_N, located in an arbitrary number of anisotropic sub-regions. Dijkstra's algorithm obeys the general search rules as follows to determine the minimum propagation time from a given start node to every node in the system.

1. Assign every node in the system an infinite propagation time except for the start node (zero propagation time).

2. Mark all nodes as 'unvisited' and select the start node (i.e. mark it as the current node)

3. Consider all adjacent nodes (i.e. neighbour nodes) to the current node and update the corresponding propagation time to each dependent upon the local propagation velocity and the distance from the current node, overwriting the previous propagation time associated with that node if less (i.e. for the start node, the propagation time to any node

13

will always be less than its initialisation value of infinity).

4. Set the new current node to be the node within the considered neighbour nodal set with the minimum associated propagation time and repeat steps 3-5.

5. Repeat until the unvisited set is empty at which point terminate the algorithm.

Nodes may be allocated to an imaging area in a regular arrangement or randomly distributed. However, there are a number of reasons why the use of a random nodal network is preferable. Firstly, the use of a regular nodal arrangement can lead to large time-of-flight errors as preferential nodal pathways are created due to the regularity of the nodes. On the other hand, use of a random nodal network introduces a 'noise' error on the time-of-flight that is both predictable and significantly smaller than the maximum time-of-flight errors due to use of a regular nodal network. Secondly, a random nodal distribution is able to conform to irregular geometries far more easily than a regular nodal arrangement, such as V-welds, curved components or buttering layers. Given that these are the principal target applications for use of the model described in this paper, a random nodal network is used. Previous work by the authors [26] also included the optimisation of various parameters associated with the accurate operation of the Dijkstra and A* algorithms, including the 'jump radius' that governs how far a ray may 'jump' while propagating between nodes.

Fundamental to the operation of the A* algorithm, is the concept of 'total cost', $T(n)$, defined as:

$$T(n) = g(n) + h(n) \tag{10}$$

14

where n is the node under consideration and $h(n)$ is the heuristic cost. The heuristic cost is composed of two parts: the heuristic time, t_h, and the heuristic weight, η, and is given as:

$$h(n) = \eta t_h \tag{11}$$

The heuristic time describes the propagation time from the node under consideration to the finish node and is given as the Euclidean distance divided by a reference velocity, c, as:

$$t_h = \frac{\sqrt{(x - x_g)^2 + (z - z_g)^2}}{c} \tag{12}$$

where x, z are the co-ordinates of the node under consideration, and x_g, z_g are the co-ordinates of the finish node. The heuristic weight is able to strengthen or weaken the influence of the heuristic calculation on the progression of the algorithm and varies from 0 i.e. nodal-dominated with no consideration of heuristic costs (i.e. Dijkstra's algorithm), to infinity i.e. heuristic-dominated with no consideration of nodal costs (i.e. a weighted depth-first search). Contrary to Dijkstra's algorithm, the A* algorithm can terminate before all nodes have been visited, and therefore a globally optimal solution cannot be guaranteed unless the choice of heuristic is admissible i.e. it never over-estimates the cost of reaching the finish node. With the correct choice of heuristic and a carefully chosen weight to ensure its admissibility, it has been shown that the A* algorithm can reduce computational time with no impact upon accuracy as compared to Dijkstra's algorithm [26, 33].

With regards to the inspection of a defect in a component, the incident, θ_{inc}, and scattering, θ_{sc}, angles from the defect are calculated by taking the mean angle from the set of J nodes that constitute the final intermediate

15

ray-jumps before incidence upon the defect, where J is an arbitrary number selected by the user. This was found to be necessary due to the random nodal allocation procedure as described in Section 3.2 leading to an unavoidable variation in the defect incident and scattering angles for multiple realisations of the same simulation. The variance was considered to be a non-physical attribute of the specific ray-tracing procedure, and therefore the averaging procedure was implemented. The average angle is calculated as the arithmetic mean of each angle, $\theta_j = \theta_{1...J}$, formed by a connection of the corresponding ray-trace node, $N_{1...J}$, to the defect node, N_{defect}, as:

$$\theta_{inc,sc} = \frac{\sum_{j=1}^{J} \theta_j}{J} \tag{13}$$

The selected J must be large enough to reduce the non-physical incidence and scattered angle variation, but small enough such that the curvature of the ray is not 'averaged out' (it can be seen that in the limiting case, if J is set to the number of nodes included in the ray-trace, then the incident and scattered angle will be equivalent to the isotropic case). Therefore, as a first approximation, J was set to 4 for all simulations in this paper as this was found to provide a good balance between reduction of the angular variation and maintenance of the ray curvature. On average, this corresponded to an averaging procedure over the final 5 mm propagation distance of the ray. Figure 3 illustrates the averaging procedure for $j = 3$.

It should be noted that the A* algorithm only calculates the time-of-flight of a ray between two arbitrary points, and therefore does not predict other anisotropy effects such as material attenuation due to a modified beam-spread or grain-scattering effects. However, this is considered to be acceptable given that the purpose of the model is to simulate defect misloca-
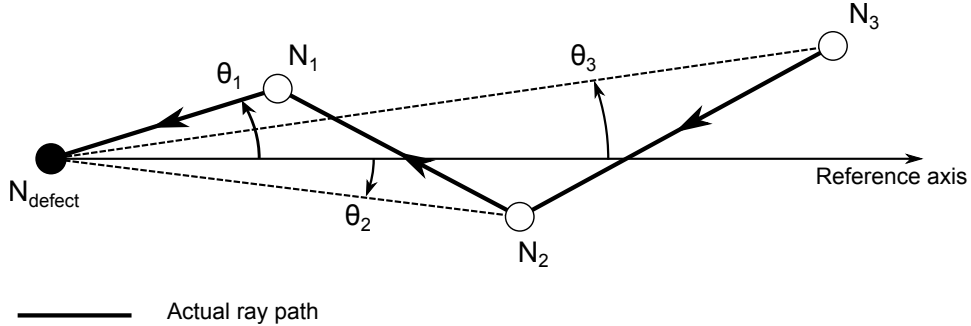
Figure 3: Schematic showing the angle averaging procedure for incident and scattering angles on the simulated defect.

tion and aberration due to beam-steering and phase aberration effects, both of which are independent of material attenuation effects. It is anticipated that future versions of the model will incorporate material attenuation effects to provide a more complete description of image degradation due to propagation through anisotropic austenitic steel welds.

3.3. Defect simulation

To simulate the scattering behaviour of an arbitrary defect, the beam-steering simulation framework uses FEM-generated scattering matrices (or S-matrices). In general, an S-matrix is a measurement of the far-field scattering amplitude from a scatterer as a function of the incident and scattering angle, and the wavelength. S-matrices can be generated through both experimental methods [34, 35] and simulation [34, 36, 28, 37, 38, 39, 35], and provide a robust and efficient method to obtain the complete scattering behaviour from a scatterer of arbitrary size and shape.

FEM-generated S-matrices have been widely used in the literature for a variety of ultrasonic scattering problems. Zhang et al. [34] proposed a time-domain FEM modeling procedure to calculate the far-field scattering amplitude and phase from a variety of crack-like defects and compared
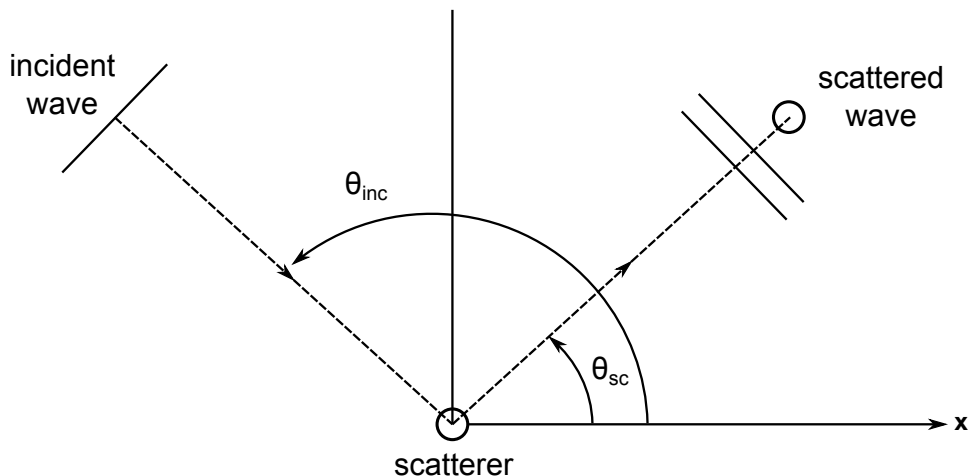
17

Figure 4: Schematic to illustrate the definitions of terms used in the 2-D S-matrix calculations.

these to experimentally measured S-matrices using an ultrasonic array to enable defect characterisation. Bai et al. [35] conducted a similar study but compared experimentally measured S-matrices to a database of simulated S-matrices, using correlation coefficients and similarity metrics to characterise the defect. Wilcox and Velichko adapted the S-matrix formalism to the frequency-domain [36] with application to arbitrarily-shaped defects embedded in a generally anisotropic medium [28] and near-surface and surface-breaking defects [37]. Moreau et al. [38] explored the use of FEM-generated S-matrices to characterise irregular shaped defects in pipes with particular application towards guided wave scattering problems. More recently, Velichko and Wilcox [39] introduced non-reflecting boundary conditions into the FEM model used to calculate the S-matrix to significantly reduce the computation time.

The FEM-generated S-matrix methodology is based on an integral representation of a wave field in a homogeneous anisotropic medium incident on

an arbitrary-shaped scatterer and can be implemented in both a 2-D and 3-D domain. Figure 4 illustrates the use of terms in the S-matrix calculations in the 2-D case and the angular convention used in this thesis. An incident wavefield, $U_{inc}(\omega)$, is incident at an angle, θ_{inc}, as measured from the positive x-axis. A receiver is also positioned in the far-field of the scatterer at a distance, r, from the scatterer and receives scattered waves at an angle of θ_{sc} as also measured from the positive x-axis. As such, the scattered wavefield, u_{sc}^{pq}, for incident mode type, p, and scattered mode type, q, is given by:

$$u_{sc}^{pq} = S^{pq}(\omega, \theta_{inc}, \theta_{sc}) \left(\frac{2\pi}{k_q r} \right) e^{ik_q r} U_{in}(\omega) u^q \qquad (14)$$

where S^{pq} is the 2-D S-matrix, k_q is the wavelength of the scattered wave mode, u^q is the scattered wave mode and α governs the beam-spreading law. Note that $\alpha = \frac{1}{2}$ for 2D bulk waves and 3D guided waves, and $\alpha = 1$ for 3D bulk waves. The scattered amplitude is normalised to that which would be received if the scatterer and monitoring point were separated by one scattered wavelength. Figure 5 illustrates an example S-matrix for a 4 mm smooth planar slot, indicating the absolute far-field scattering amplitude as a function of the incident and scattering angles at a frequency of 2 MHz. Note that incident and scattering angles are defined from a line bisecting the centre of the slot and lying perpendicular to its length.

3.4. Beam-simulation and imaging

The 2-D semi-analytical beam-steering model has a high degree of flexibility in terms of the type and geometry of the component to be inspected, and the probe to be used (e.g. single-element transducer or contact/wedge-mounted phased array). Considering a contact array inspection of a weld,
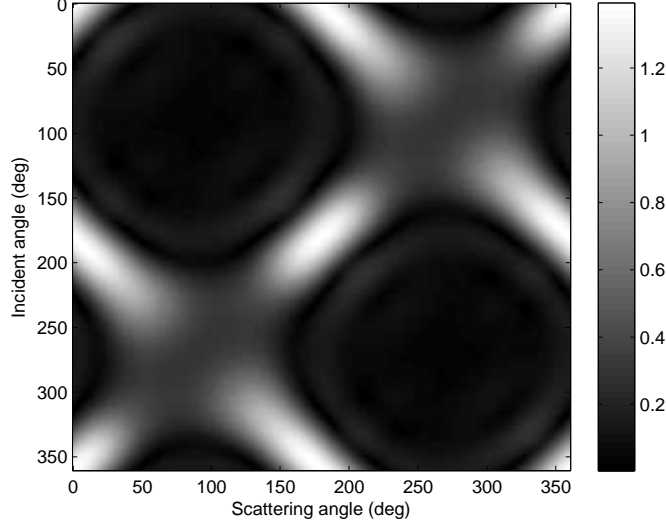
Figure 5: Example S-matrix detailing the absolute scattered amplitude for a 4 mm planar slot at a frequency of 2 MHz.

the frequency domain response for an arbitrary scatterer, $F_{contact}(\omega)$, is given by:

$$F_{contact}(\omega) = \sqrt{\frac{\lambda}{r_{tx}r_{rx}}} e^{-i\omega(t_{tx}+t_{rx})} D(\omega, \theta_{tx}) D(\omega, \theta_{rx})$$
$$I(\omega)^2 S^{pq}(\omega, \theta_{inc}, \theta_{sc}) \tag{15}$$

where λ is the wavelength, r_{tx} and r_{rx} are the propagation distances from the transmitting and receiving element to the defect, respectively, t_{tx} and t_{rx} are the times-of-flight from the transmitting and receiving element to the defect obtained via ray-tracing, respectively, D is the directivity function of the array element, θ_{tx} and θ_{rx} are the ray angles as taken from the normal to the transmitting and receiving elements, respectively, $I(\omega)$ is the impulse response function of the element and S^{pq} is the far-field defect scat-

20

tering amplitude as given by the corresponding S-matrix, with incident and scattering angles as defined in Section 3.2. For a wedge-mounted phased array, Equation (15) is modified to yield the frequency domain response of the defect, $F_{wedge}(\omega)$, as:

$$F_{wedge}(\omega) = \sqrt{\frac{\lambda}{r_{tx}^E r_{rx}^E}} e^{-ik(r_{tx}^E + r_{rx}^E)} D(\omega, \theta_{d,tx}) D(\omega, \theta_{d,rx})$$

$$S^{pq}(\omega, \theta_{inc,tx}, \theta_{sc,rx}) T(\theta_{1,tx}, \theta_{2,tx}) T(\theta_{2,rx}, \theta_{1,rx}) I(\omega)^2$$

(16)

where θ_1 and θ_2 are the incident and refracted angles at the wedge/steel interface, θ_d is the ray angle as measured from the normal to the array, T and R are the transmission and reflection coefficients at the wedge/steel interface [40], and r_{tx}^E and r_{rx}^E are the effective propagation distances from the transmitter and receiver to the defect. The effective propagation distance accounts for the fact that following refraction at the wedge/steel interface, wave-fronts are no longer cylindrical in shape and the beam-spread is modified accordingly. It is calculated based on an approximation derived by Johnson [41]:

$$r^E = r_1 \frac{\cos \theta_2}{\cos \theta_1} + r_2 \frac{c_2}{c_1} \frac{\cos \theta_1}{\cos \theta_2}$$

(17)

where r is the propagation distance and c is the velocity. Note that subscripts 1 and 2 refer to the medium either side of the interface.

The beam-steering model described is used to simulate the full-matrix of transmit-receive signals for a given array inspection scenario. In this paper, the Total Focusing Method (TFM) is used for imaging as developed by Holmes et al. [42]. To calculate the mislocation and amplitude decrease of

Table 1: Material elastic properties for the transversely isotropic type-308 austenitic weld metal [9].

Material Parameter	Value (Nm^{-2})
C_{11}	263 x 10^9
C_{12}	98 x 10^9
C_{13}	145 x 10^9
C_{33}	216 x 10^9
C_{44}	129 x 10^9
C_{66}	82.5 x 10^9

the defect response, firstly the isotropic equivalent simulation is run (assuming no weld anisotropy is present), and then the anisotropic ray-tracing simulation is run (assuming weld anisotropy is present). For the isotropic case, ray-tracing is performed using a Fermat minimum-time search, accounting for the wedge/material interface if using a wedge-mounted array. The defect mislocation can be given by two components; the lateral mislocation, x_{mis}, equivalent to the difference between the x-coordinates of the location of the isotropic maxima, x_{iso}, and the anisotropic maxima, x_{aniso}, and the through-wall mislocation, z_{mis}, equivalent to the difference between the z-coordinates of the location of the isotropic maxima, z_{iso}, and the anisotropic maxima, z_{aniso}. Note that for the co-ordinate convention used in this paper, a positive x_{mis} corresponds to a mislocation in the positive x-axis, while a positive z_{mis} corresponds to a mislocation in the positive z-axis. The absolute mislocation, d_{mis}, is given as the Euclidean distance between the location of the isotropic and anisotropic defect positions. The defect image amplitude change, P_{diff}, is equivalent to the difference between the peak amplitude of the defect in the isotropic image, P_{iso}, and the corresponding anisotropic image, P_{aniso}, in decibels (dB) as:

Table 2: MINA parameters for the 55 mm thick austenitic V-weld validation test-piece.

MINA Parameter	Value
R_L	0.165
R_V	0.311
θ_B	17.08°
θ_C	0.82°

$$P_{diff} = 20 \log_{10} \left(\frac{P_{aniso}}{P_{iso}} \right) \tag{18}$$

4. Validation

To provide validation of the beam-steering model, the position of an array-generated focal spot was measured in experiment, and then recreated in simulation. Figure 6 details the experimental arrangement used for validation indicating two linear arrays with 64 elements each of 1.5 mm pitch at a centre frequency of 2 MHz: array A and array B. Both arrays were held a fixed lateral distance apart, $x_{sep} = 90$ mm, using a simple rig and placed firstly over 304 SS parent material (position 1) and then asymmetrically over a 308 SS V-weld (position 2), with weld dimensions as given in Figure 7, so as to maximise the distance of propagation through the weld. Material properties for the weld are given in Table 1.

At both positions, array A was focused onto the surface of array B via the back-wall. This focal position was moved incrementally across each element of array B. For each focal spot position, the absolute amplitude across array B was measured at each element such that the position of the focal maxima could be extracted. The difference between the position of the focal maxima during isotropic propagation and that obtained for anisotropic weld propagation was then calculated to give the 'focal-spot shift', Q, due to the
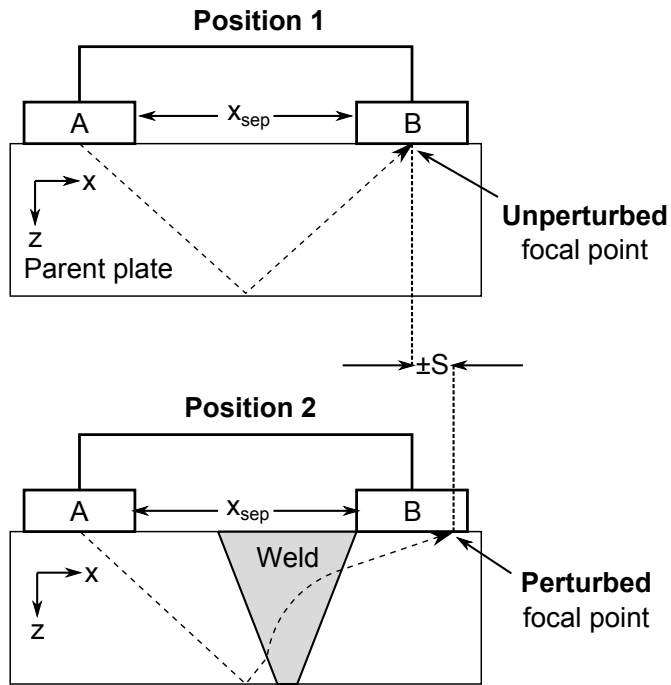
Figure 6: Schematic showing the positioning of the rig so as to allow measurement of the focal spot perturbation due to weld anisotropy. Note that the test-piece has been 'split' into separate sections for illustrative purposes.
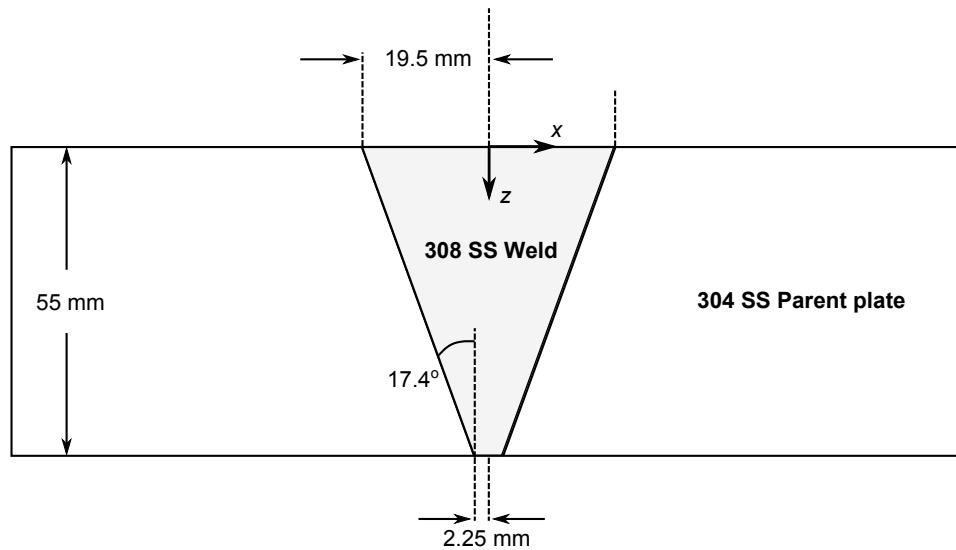

Figure 7: Schematic of the 308 SS V-weld used for validation of the beam-steering framework.

presence of weld anisotropy. Note that Q can be either positive or negative dependent on whether the focal-spot movement was to the right or to the left, respectively. To recreate the experimental weld in simulation, a macrograph of the weld was analysed and coupled with knowledge of the welding parameters to yield the corresponding MINA weld-map, with parameters as given in Table 2 [43]. Following analysis of the macrograph, an anisotropy sub-region size of 1 mm^2 was used to approximate to the observed rate of change of anisotropy within the weld. Figure 8 details the focal spot movement as a function of the focal element position on array B, with error bars equal to half of the array element pitch. Both simulated and experimental data show good trend agreement as the focal element is adjusted, with a negative Q shift at lower focal elements and a positive Q shift at higher focal elements. For example, when array A is focused on element 27 of array B, a 1.5 mm positive Q shift is recorded in both simulation and experiment. Results do, however, indicate a degree of fluctuation which is thought to be due in part to the inherent variation of the weld microstructure and the errors associated with weld recreation in experiment using the MINA model. Beyond a focal element of 30, a focal maxima across array B could not be reliably extracted due to the reduced ability of the array to focus at higher beam angles leading to multiple maxima in the observed amplitude profile, and have therefore been excluded. Furthermore, results below a focal element of 15 have been excluded such that a sufficiently large amplitude profile across array B could be analysed and a focal spot maximum extracted.
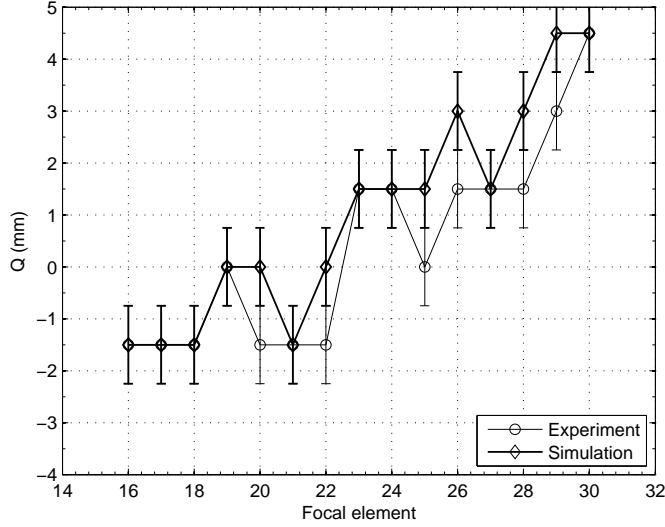
Figure 8: Focal spot shift as a function of the focal element on array B. The x-axis indicates the desired location of the focus on array B and the y-axis indicates the difference in the location of this focus due to the weld anisotropy.

5. Parametric studies

To provide examples of the operation of the beam-steering model, a number of parametric studies are detailed. These are chosen to reflect the flexibility of the individual components of the model, with particular reference given to the corresponding computation time. The primary purpose of the model is to allow the assessment of image degradation due to weld anisotropy such that the inspection development process may be informed and adjusted as necessary. All parametric studies are performed on a simulated weld intended to represent the experimental weld used during validation in Section 4, and use the MINA parameters as detailed in Table 2, unless otherwise specified. Furthermore, ray-tracing was performed using the A* algorithm at a heuristic weight of 0.8 to ensure both its admissibility and a rapid computation speed [26]. This was verified through comparison
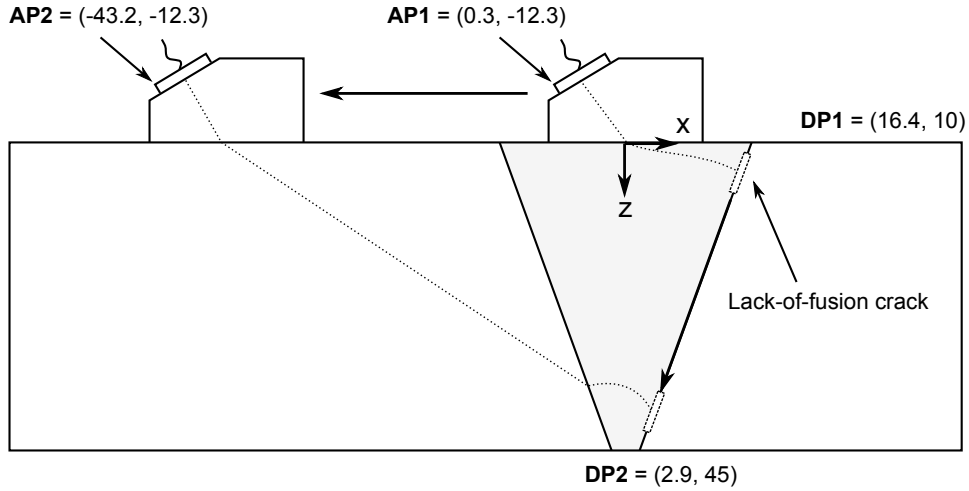
26

Figure 9: Simulated inspection setup for the defect position parametric study.

with Dijkstra's algorithm as detailed in Section 3.2.

5.1. Variation of Defect Position

Figure 9 details the simulated inspection setup for analysis of the effect of defect position on the image degradation of a 4 mm planar smooth lack-of-fusion crack on the right-hand fusion face. All simulations were performed using a 32 element 0.78 mm pitch, 2 MHz wedge-mounted array with a wedge angle of 16°. The weld geometry is identical to that shown in Figure 7. The centre of the crack was varied from position DP1, $(x, z) = (16.4, 10)$ mm to position DP2, $(x, z) = (2.9, 45)$ mm in $z = 1$ mm increments parallel to the fusion-face. The probe was moved accordingly from position AP1, $(x, z) = (0.3, -12.3)$ mm to Position AP2, $(x, z) = (-43.2, -12.3)$ mm, where the position corresponds to the location of the first element of the array, and such that the beam from the centre of the array aperture was normally incident on the defect centre, nominally at 43° assuming isotropic propagation and excitation of the array with no applied delay laws.

27
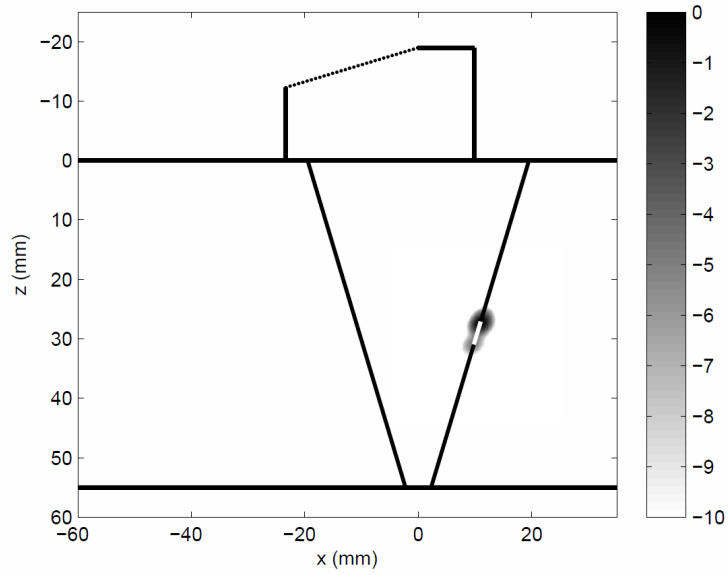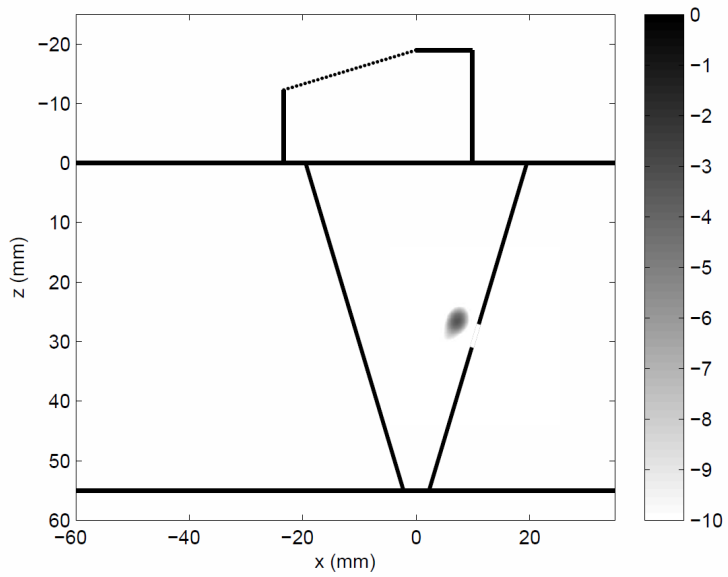
Figure 10: Example TFM images for (a) isotropic propagation and (b) anisotropic propagation, indicating the corresponding defect mislocation and degradation. The dynamic scale is given in dB.

28

Figure 10 illustrates one iteration of the beam-steering simulation framework indicating both the isotropic imaging case (Figure 10a) and the anisotropic imaging case (Figure 10b) when the probe is located on the top of the weld at a first element position of $(x, z) = $ (-22.6, -12.3) mm. For isotropic propagation, the lack-of-fusion crack is detected and positioned accurately, exhibiting clear responses from the top and bottom tip of the defect. The anisotropic image as given in Figure 10b is normalised against the peak amplitude of the isotropic image as given in Figure 10a and exhibits an amplitude decrease, $P_{diff} = $ -3 dB, and an absolute mislocation, $d_{mis} = $ 4 mm. The direction of mislocation is principally confined to the x-axis, appearing to be located nearer to the weld centre-line than reality, and furthermore, the response from the bottom tip is now undetectable within the given dynamic range.
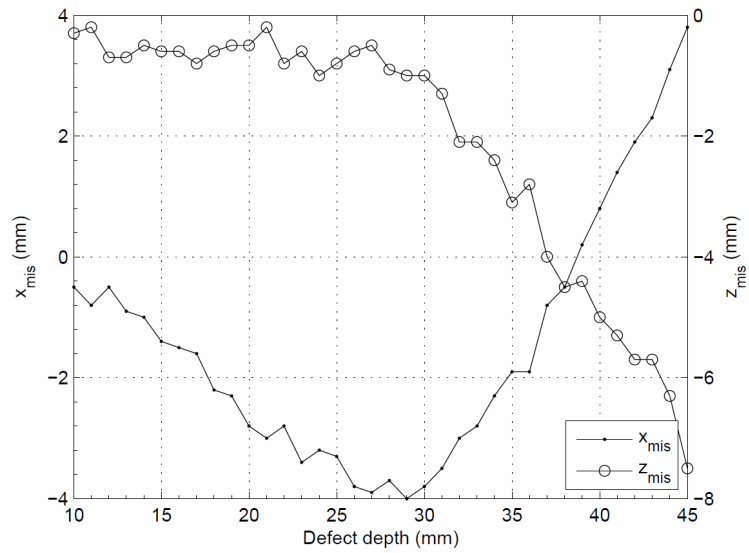
Figure 11a details the absolute defect mislocation and amplitude change (in dB) as a function of the defect depth. An initially large $P_{diff} = $ -10 dB at a defect depth of 10 mm is obtained, however as the defect depth is increased, a reduction in P_{diff} is observed. The somewhat erratic variation of P_{diff} as the defect depth is increased may be attributed to the precise nature of the anisotropy, leading to the existence of preferential ray-paths for certain positions of the array. This is demonstrated as a degree of fluctuation of P_{diff} between different positions of the array. As the defect depth is increased from 10 to 30 mm, the wedge-mounted array is positioned such that the entire beam-width overlaps with the top of the weld, and this is accompanied by a steadily increasing P_{diff}. Above a defect depth of 30 mm, however, the behaviour of P_{diff}, again, becomes more erratic. Above this depth, the wedge-mounted array is positioned such that the beam is travelling through both the parent material immediately adjacent to the

29

weld and the top of the weld itself. Since the beam is subject to different ray-paths dependent upon whether it enters parent material or weld material initially, it is hypothesised that this phenomenon leads to a significantly different beam-shape at each position of the probe, leading to a somewhat erratic variation of P_{diff}. With regards to defect mislocation, an initial $d_{mis} < 1$ mm at a defect depth of 10 mm is observed, with a steady increase as the defect depth is increased to a maximum $d_{mis} = 8$ mm at a defect depth of 45 mm. The curve, however, exhibits a point of inflection around a defect depth of 35 mm. To further explore this, the respective horizontal, x_{mis}, and through-wall, z_{mis}, components of mislocation are calculated as given in Figure 11b. At a defect depth of 10 mm, both a small x_{mis} and z_{mis} are observed, leading to a small d_{mis} as indicated in Figure 11a. As the defect depth is increased up to 30 mm, there is a substantial increase in x_{mis} (a negative x_{mis} corresponds to a mislocation towards the left-hand side), and an associated small increase in z_{mis}, indicating that for inspection through the top of the weld, the horizontal mislocation is the dominant factor. However, above a defect depth of 30 mm, x_{mis} decreases rapidly and becomes positive (i.e. mislocated towards the right-hand side), in addition to a rapidly increasing z_{mis} e.g. at a defect depth of 45 mm, a through-wall mislocation of over 7 mm is observed. It can therefore be seen that the characteristic shift of x_{mis} produces the inflection point in the d_{mis} as given in Figure 11a. The rapidly increasing through-wall (z-axis) mislocation presents the most concern from a structural integrity perspective, as its negative value means that a defect ligament may be misinterpreted, for example a surface-breaking defect could be misclassified as an embedded defect.

For the case considered, each run of the model (i.e. simulation of a FMC
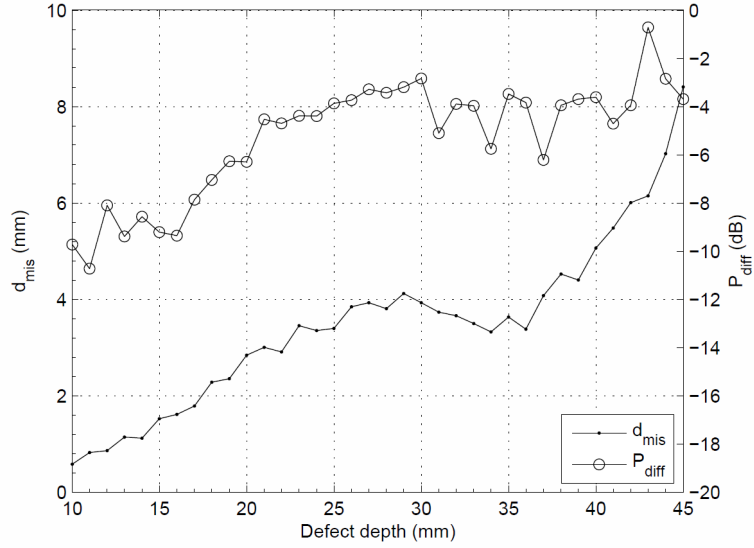
Figure 11: (a) Absolute defect mislocation and amplitude change and (b) horizontal and through-wall defect mislocation as a function of defect depth.

data-set and subsequent imaging) took a total of 193 seconds to run on a Dell T5610 Precision Workstation (Intel® Dual Xeon E5-2600 v2, 32 cores, 2.6 GHz, 128 GB RAM). Assuming a free-mesh refinement of 30 nodes per wavelength, an equivalent 2D FEM simulation would contain between 450000 and 600000 nodes for the smallest and largest simulation regions, respectively, as defined by the first-element and weld positions as given in Figure 9. This equates to an average of 525000 nodes per simulation, or approximately 1 million degrees of freedom in a 2D simulation. A finite element model using these parameters was run on an identical workstation using the finite element software package, ABAQUS®, taking approximately 16 hours to compute the FMC data-set.

5.2. Variation of Weld Anisotropy

Due to the fact that grain formation is an inherently random process during weld solidification (albeit subject to mechanisms that influence the size, shape and orientation of the grains), the grain structure at different positions along a weld cannot be assumed to be identical along the weld. It therefore cannot be said with certainty that the response from a defect at a certain position along the weld will be the same as an identical inspection at a different position. The observed variation may be used to identify the impact of microstructural variation on a given inspection and used to inform the inspection development process e.g. analysis of the standard deviation and range of defect mislocation and amplitude changes following execution of a statistically significant number of iterations.

Figure 12 details the simulated inspection setup for analysis of the impact of weld anisotropy variation upon imaging. All simulations were performed using a 32 element 0.78 mm pitch, 2 MHz array located to the left-hand-

Table 3: Variation of MINA parameters for the anisotropy distribution parametric study.

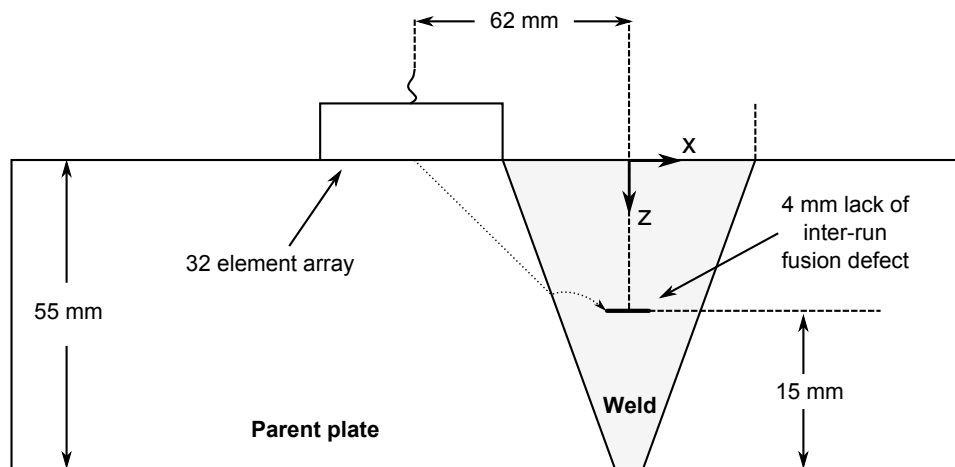| MINA Parameter	Variation (±)	Min. Value	Actual Value	Max. Value
R_L	0.15	0.015	0.165	0.315
R_V	0.15	0.161	0.311	0.461
θ_B	15°	2.08°	17.08°	32.08°
θ_C	15°	−14.18°	0.82°	15.82°

Figure 12: Simulated inspection setup for the anisotropy distribution parametric study.

side of the weld, with dimensions as given in Figure 7. A 4 mm planar smooth lack-of-inter-run fusion defect was located at $(x, z) = (0, 40)$ mm within the weld material, with material parameters as given in Table 1. To simulate variation of the weld microstructure along the circumferential weld direction, the weld pass angles, θ_B and θ_C, and re-melting rates, R_L and R_V, were chosen at random from a normal distribution of random values generated around the actual MINA parameters as given in Table 2. Bounds of variation were imposed on the extrema of each normal distribution so as to be representative of the maximum variation of the MINA parameters that may be expected for an actual welded test-piece. Ideally, the bounds of variation should be informed through analysis of a selection of macrographs from different weld positions. A weighting can then be applied to measured differences to account for undersampling errors due to only considering a small number of weld macrographs; a likely scenario due to the inherent difficulty in obtaining a large number of weld macrographs at different positions. For the case considered, however, it was not possible to obtain a selection of macrographs at different circumferential weld positions and as such, reasonable bounds of variation were chosen and are given in Table 3.

The beam-steering framework was executed for 300 random realisations of the MINA parameters within the bounds of variation, with results in the form of histogram bar-charts detailed in Figure 13. As indicated in Figure 13a, a mean absolute mislocation, $\bar{d}_{mis} = 9.2$ mm was obtained, with a range of 1.4 mm. Although the absolute mislocation is large for this particular case-study, the variation of the mislocation due to variation of the weld anisotropy is relatively small in comparison. Analysis of the respective horizontal and through-wall mislocation components of the absolute mislocation is detailed in Figure 13b and Figure 13c. Here, a mean horizontal
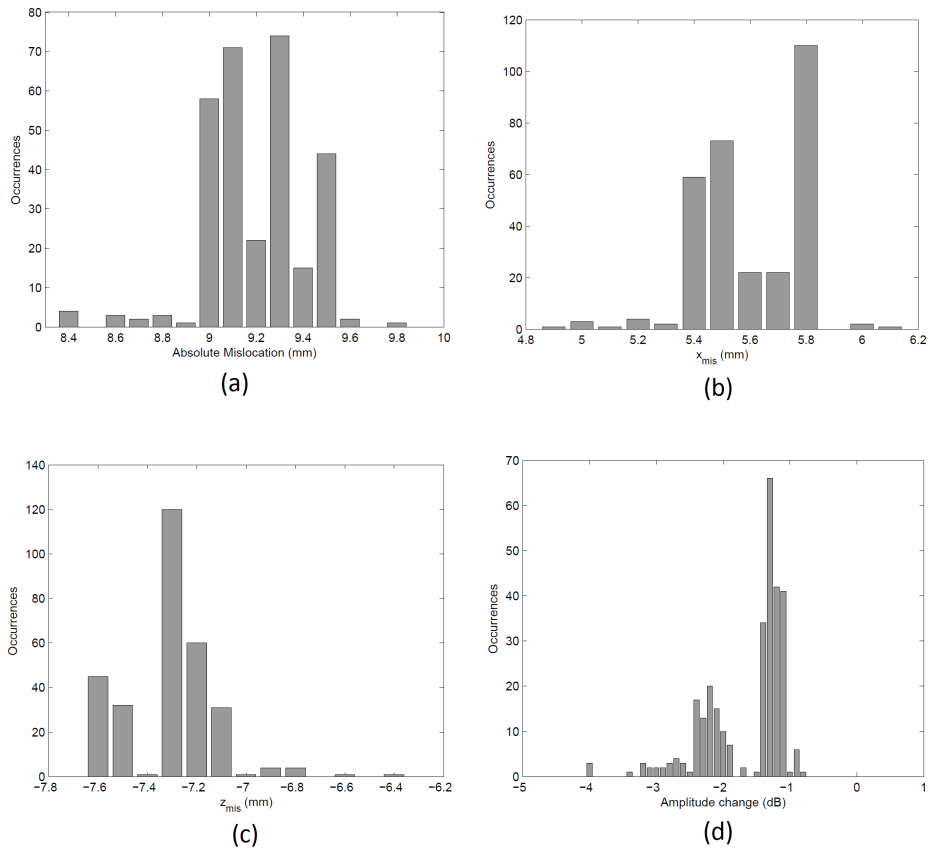
34

Figure 13: Histogram bar-charts detailing (a) absolute mislocation (b) horizontal mislocation (c) through-wall mislocation and (d) amplitude change for 300 realisations of the beam-steering framework.

mislocation, $\bar{x}_{mis}$ = 5.6 mm and a mean through-wall mislocation, $\bar{z}_{mis}$ = -7.3 mm was obtained. Again, the magnitude of the component mislocation, in particular the through-wall component, is of particular concern from a structural integrity standpoint, however the associated variation over the data-set is small. Figure 13d details the distribution of the observed amplitude change, indicating a trimodal distribution with the principal maxima located around -1.3 dB, and smaller local maxima at -2.2 and -2.7 dB. The observed multimodal distribution implies the existence of three 'preferential' sets of ray paths for the given simulated inspection setup. In this case, although the choice of MINA parameters is essentially taken at random from pre-defined bounds of variation, over a large enough number of realisations, this is manifested as three distinct amplitude changes in the final defect image, of varying impact and probability of occurrence. However, the distinct trimodal distribution as exhibited in Figure 13d, is not observed in the mislocation analysis, as given in Figures 13a to 13c. Instead, it can be seen that the histograms, while not observing a normal distribution, demonstrate a degree of fluctuation, most notably demonstrated by the increased occurrences in the -7.3 mm through-wall mislocation bin as given in Figure 13c. Again, it is likely that this is a manifestation of a preferential ray-path associated with the given MINA parameters and weld-map. From an inspection development standpoint, the identification, analysis and quantification of a multimodal distribution means that image degradation due to weld anisotropy variation can be predicted. Such a result highlights the importance of a model of this nature, and the added insight that can be provided with regards to potential defect degradation during inspection of a weld. For the case considered, each iteration of the model (i.e. collection of a FMC data-set and subsequent imaging) took a total of 160 seconds to

36

run on an equivalent workstation to that detailed in Section 5.1. Assuming a mesh refinement of 30 nodes per wavelength and a simulation area equivalent to that given in Figure 12 (i.e. a square region encompassing the weld region and the left-most element of the contact phased array), an equivalent FEM simulation would contain roughly 375000 nodes, or 750000 degrees of freedom assuming a 2D simulation. A finite element model using these parameters was run on an identical workstation using the finite element software package, ABAQUS®, taking approximately 8 hours to compute the FMC data-set.

6. Conclusions

This paper has detailed the development and operation of a semi-analytical beam-steering model for the analysis of defect mislocation and aberration due to anisotropic austenitic weld material. The model uses a rapid ray-tracing algorithm, the A* algorithm, to calculate the path of ultrasound through a predetermined weld anisotropy distribution and calculates the scattered response from a given defect using an efficient FEM method. This is then compared to the isotropic equivalent simulation and metrics such as defect mislocation and aberration due to the presence of weld anisotropy are calculated. A number of parametric studies are presented aimed at the inspection of a typical austenitic weld, to exhibit the potential for use of such an algorithm when applied to real inspection applications. Variation of the defect and probe position indicated variation of the absolute mislocation from less than 1 mm to over 8 mm for a planar slot defect located at the top and bottom of the weld fusion-face, respectively. Furthermore, variation of the weld anisotropy in a Monte-Carlo study indicated that although the

37

absolute mislocation was large at over 9 mm, variation of the mislocation for different weld microstructures was small.

Due to the high computational efficiency of the beam-steering model, there is significant potential to include the model within an optimisation framework such that a particular degradation metric could be minimised against the variation of a single or multiple inspection parameters. For instance, during an inspection development stage for a particular weld inspection, the weld could be reconstructed in simulation through use of the MINA model, validation defects simulated through use of the appropriate S-matrices, and the probe position and characteristics optimised to reduce upon the corresponding image aberration for a particular defect location. Optimisation of the inspection would enable an improved component life and reduce associated operational costs.

Acknowledgments

References

[1] R. J. Hudgell, B. S. Gray, The ultrasonic inspection of austenitic materials - State of the Art Report, Tech. rep., Risley Nuclear Power Development Laboratories (1985).

[2] B. A. Auld, Acoustic Fields and Waves in Solids, Wiley, 1973.

[3] C. Gueudre, L. Le-Marrec, J. Moysan, B. Chassignole, Direct model optimisation for data inversion. Application to ultrasonic characterisation of heterogeneous welds, NDT&E International 42 (2009) 47–55.

[4] B. Puel, D. Lesselier, S. Chatillon, P. Calmon, Optimization of ultrasonic arrays design and setting using a differential evolution, NDT&E International 44 (2011) 797–803.

[5] J. Zhang, B. W. Drinkwater, P. Wilcox, Monte Carlo inversion of ultrasonic array data to map anisotropic weld properties, IEEE Transactions on Ultrasonics, Ferroelectrics and Frequency Control 59 (2012) 2487–2497.

[6] Y. Humeida, P. D. Wilcox, M. D. Todd, B. W. Drinkwater, A probabilistic approach for the optimisation of ultrasonic array inspection techniques, NDT&E International 68 (2014) 43–52.

[7] P. Fellinger, R. Marklein, K. J. Langenberg, S. Klaholz, Numerical modeling of elastic wave propagation and scattering with efit - elastodynamic finite integration technique, Wave Motion 21 (1995) 47–66.

[8] S. Halkjaer, M. P. Sorenson, W. D. Kristensen, The propagation of ultrasound in an austenitic weld, Ultrasonics 38 (2000) 256–261.

[9] J. A. Ogilvy, Ultrasonic beam profiles and beam propagation in an austenitic weld using a theoretical ray-tracing model, Ultrasonics 24 (1986) 337–347.

[10] R. Hannemann, R. Marklein, K. J. Langenberg, C. Schurig, B. Kohler, F. Walte, Ultrasonic wave propagation in real-life austenitic v-butt

welds: Numerical modeling and validation, Review of Progress in Quantitative Nondestructive Evaluation 509 (2000) 145–152.

[11] K. J. Langenberg, R. Hannemann, T. Kaczorowski, R. Marklein, B. Koehler, C. Schurig, F. Walte, Application of modeling techniques for ultrasonic austenitic weld inspection, NDT&E International 33 (2000) 465–480.

[12] B. Chassignole, D. Villard, M. Dubuget, J. C. Baboux, R. El Guerjouma, Characterization of austenitic stainless steel welds for ultrasonic ndt, Review of Progress in Quantitative Nondestructive Evaluation 509 (2000) 1325–1332.

[13] A. Apfel, J. Moysan, G. Corneloup, T. Fouquet, B. Chassignole, Coupling an ultrasonic propagation code with a model of the heterogeneity of multipass welds to simulate ultrasonic testing, Ultrasonics 43 (2005) 447–456.

[14] B. Chassignole, V. Duwig, M.-A. Ploix, T. Fouquet, Modelling the attenuation in the ATHENA finite elements code for the ultrasonic testing of austenitic stainless steel welds, Ultrasonics 49 (2009) 653–658.

[15] B. Chassignole, R. El Guerjouma, M.-A. Ploix, T. Fouquet, Ultrasonic and structural characterization of anisotropic austenitic stainless steel welds: Towards a higher reliability in ultrasonic non-destructive testing, NDT&E International 43 (2010) 273–282.

[16] S. Shahjahan, F. Rupin, T. Fouquet, A. Aubry, A. Derode, Structural noise and coherent backscattering modelled with the ATHENA 2D fi-

nite elements code, Proceedings of the Acoustics 2012 Nantes Conference (2012) 2645–2650.

[17] C. Rose, F. Rupin, T. Fouquet, B. Chassignole, Athena 3d: A finite element code for ultrasonic wave propagation, Journal of Physics: Conference Series - 12th Anglo-French Physical Acoustics Conference 498 (2014) 1–11.

[18] M. Darmon, P. Calmon, B. Bele, An integrated model to simulate the scattering of uultrasound by inclusions in steels, Ultrasonics 42 (2004) 237–241.

[19] B. R. Julian, D. Gubbins, Three-dimensional seismic ray-tracing, Journal of Geophysics 43 (1977) 95–114.

[20] G. D. Connolly, M. J. S. Lowe, J. A. G. Temple, S. I. Rokhlin, Correction of ultrasonic array images to improve reflector sizing and location in inhomogeneous materials using a ray-tracing model, Acoustical Society of America 127 (2010) 2802–2812.

[21] J. A. Ogilvy, Computerized ultrasonic ray-tracing in austenitic steel, NDT International 18 (1985) 67–77.

[22] J. A. Ogilvy, The ultrasonic reflection properties of planar defects within austenitic welds, Ultrasonics 26 (1986) 318–327.

[23] A. Harker, J. A. Ogilvy, J. A. G. Temple, Modelling ultrasonic inspection of austenitic welds, Journal of Nondestructive Evaluation 9 (1990) 155–165.

[24] M. G. Silk, Computer model for ultrasonic propagation in complex orthotropic structures, Ultrasonics 19 (1981) 208–212.

[25] V. Schmitz, F. Walte, S. V. Chakhlov, 3D ray-tracing in austenite materials, NDT&E International 32 (1999) 201–213.

[26] O. Nowers, D. J. Duxbury, J. Zhang, B. W. Drinkwater, Novel raytracing algorithms in NDE: Application of Dijkstra and A* algorithms to the inspection of an anisotropic austenitic steel weld, NDT&E International 61 (2014) 58–66.

[27] P. E. Hart, N. J. Nilsson, B. Raphael, A formal basis for the heuristic determination of minimum cost paths, IEEE Transactions on Systems Science and Cybernetics 4 (1968) 100–107.

[28] A. Velichko, P. Wilcox, A generalized approach for efficient finite element modeling of elastodynamic scattering in two and three dimensions, Journal of the Acoustical Society of America 128 (2010) 1004–1014.

[29] B. W. Drinkwater, P. Wilcox, Ultrasonic arrays for Non-Destructive Evaluation: A review, NDT&E International 39 (2006) 525–541.

[30] J. Moysan, A. Apfel, G. Corneloup, B. Chassignole, Modelling the grain orientation of austenitic stainless steel multipass welds to improve ultrasonic assessment of structural integrity, International Journal of Pressure Vessels and Piping 80 (2003) 77–85.

[31] E. Dijkstra, A note on two problems in connexion with graphs, Numerische Mathematik 1 (1959) 269–271.

[32] G. Gutin, A. P. Punnen, The Travelling Salesman Problem and its variations, Springer, 2006.

[33] I. Chabini, S. Lan, Adaptations of the A* algorithm for the computation

of fastest paths in deterministic discrete-time dynamic networks, IEEE Transactions on Intelligent Transportation Systems 3 (2002) 60–74.

[34] J. Zhang, B. W. Drinkwater, P. D. Wilcox, Defect characterization using an ultrasonic array to measure the scattering coefficient matrix, IEEE Transactions on Ultrasonics, Ferroelectrics and Frequency Control 55 (2008) 2254–2265.

[35] L. Bai, A. Velichko, B. W. Drinkwater, Ultrasonic characterisation of crack-like defects using scattering matrix similarity metrics, IEEE Transactions on Ultrasonics, Ferroelectrics and Frequency Control 62 (3) (2015) 545–559.

[36] P. Wilcox, A. Velichko, Efficient frequency-domain finite element modeling of two-dimensional elastodynamic scattering, Journal of the Acoustical Society of America 127 (2010) 155–165.

[37] A. Velichko, P. Wilcox, Efficient finite-element modelling of elastodynamic scattering from near surface and surface-breaking defects, Review of Progress in Quantitative Nondestructive Evaluation 30 (2011) 59–66.

[38] L. Moreau, A. Velichko, P. Wilcox, Accurate finite-element modelling of guided wave scattering from irregular defects, NDT&E International 45 (2012) 46–54.

[39] A. Velichko, P. Wilcox, Efficient finite element modeling of elastodynamic scattering with non-reflecting boundary conditions, Review of Progress in Quantitative Nondestructive Evaluation Proc. 1430 (2012) p142–149.

[40] J. L. Rose, Ultrasonic Waves in Solid Media, Cambridge University Press, 1999.

[41] J. A. Johnson, N. M. Carlson, D. M. Tow, Ray trace calculations of ultrasonic fields, Research in Nondestructive Evaluation 3 (1991) 27–39.

[42] C. Holmes, B. Drinkwater, P. Wilcox, Post-processing of the full matrix of ultrasonic transmit-receive array data for non-destructive evaluation, NDT&E International 38 (2005) 701–711.

[43] Z. Fan, M. J. S. Lowe, Array imaging of austenitic welds by measuring weld material map, Review of Progress in Quantitative Nondestructive Evaluation 1581 (2014) 941–947.